X. Y. Fang ^a, Z. M. Guo ^a, C. Wang ^a, X. G. Chen ^a, X. N. Chi ^b, W. Q. Liu ^c, J. O. Chen ^{a,*}

a School of Mechanical Engineering, Chengdu University, Chengdu, 610106, China

b China Industrial Control Systems Cyber Emergency Reponse Team, Beijing 100043, China

c Qingdao Institute of Bioenergy and Bioprocess Technology, Chinese Academy of Sciences, Qingdao 266101, China

The development of eco-friendly strategies for precise TiO₂ photocatalyst control remains critical for environmental remediation. Herein, oxalic acid (OA) is innovatively employed as a multiple-function modulator to synergistically regulate the crystalline phase, morphology, and size of TiO₂, achieving improved photocatalytic performance. With increasing OA concentration, the TiO₂ particle size decreased remarkably from the micrometer scale (2.58 μm) to the sub-micrometer scale (0.60 μm). At optimized OA concentration (S25), TiO₂ exhibits the minimized particle sizes, maximized specific surface area with increased active sites, and reduced charge recombination. Photocatalytic degradation rates for methyl orange (MO) and tetracycline (TC) under simulated sunlight reveal exceptional performance: S25 achieves 100% MO degradation in 30 min and 100% TC degradation in 10 min, with rate constants 4.15× and 1.40× higher than OA-free samples, respectively. This work provides a green pathway for the scalable preparation of high-performance TiO₂ photocatalysts with controllable structures, demonstrating significant application potential for industrial wastewater purification.

(Received July 8, 2025; Accepted October 10, 2025)

Keywords: Photocatalytic activity, TiO₂, Oxalic acid, Pollutant degradation, Morphology control

1. Introduction

The rapid development of global industrialization and urbanization has exacerbated the accumulation of recalcitrant organic pollutants in water bodies[1, 2]. By virtue of its green nature, high efficiency, and capability for deep mineralization of pollutants, photocatalytic technology is regarded as an innovative environmental remediation strategy to replace traditional wastewater treatment methods, which are often inefficient and carry high risks of secondary pollution[3, 4].

^{*} Corresponding author: chenjiaqi@cdu.edu.cn https://doi.org/10.15251/DJNB.2025.204.1235

Titanium dioxide (TiO₂) represents a quintessential photocatalytic material, drawing significant scientific focus due to attributes such as excellent chemical stability, absence of toxicity, and economic viability. Among its polymorphs, anatase-phase TiO₂ exhibits superior photocatalytic activity, rendering it particularly promising for practical applications[5-7]. Nevertheless, the efficiency of TiO₂ photocatalysis is strongly influenced by its crystalline phase composition[6, 8-10], particle morphology[10-13], and size [14-16]. Achieving synergistic control over these multiple dimensions remains a pivotal challenge. The performance of TiO₂ can be significantly enhanced through meticulous control of its crystalline phase stability and particle morphology[17-19].

Various acids (e.g., hydrochloric acid[20], sulfuric acid[21], hydrofluoric acid[22]) were used to modulate the morphology and structures of the TiO₂ photocatalysts. Gu et al. [23] demonstrated that nanoparticles synthesized in an acetic acid/hydrochloric acid system exhibit more uniform morphology compared to those from a nitric acid system. Andrade-Guel et al. [20] further revealed through microwave-assisted sol-gel synthesis that the hydrochloric acid system yields polymorphic TiO₂, whereas the acetic acid system enables rapid formation of pure anatase phase. Crude morphological control, substantial costs, and notable ecological risks nevertheless persist as limitations in conventional strong acid methodologies[24, 25]. The strong corrosivity of the acids often leads to particle agglomeration, non-uniform size distribution, and impurity incorporation, thereby limiting charge carrier transport efficiency[26, 27]. Consequently, devising environmentally benign and low-risk methodologies to control morphological characteristics and functional properties of TiO₂-based photocatalysts represents an essential research priority.

In this study, we aimed to simultaneously achieve enhanced crystalline phase stability of TiO₂, the construction of well-defined hexagonal prismatic morphology, and precise micro/nanoscale control. OA was innovatively utilized as a dual-functional modulator, not only significantly improving the thermal stability of the anatase phase (maintaining pure anatase structure even after high-temperature calcination) but also successfully inducing the transformation of TiO₂ particles from irregular polyhedrons into uniform hexagonal prismatic structures. Under specific C₂O₄²⁻:Ti⁴⁺ molar ratios, samples with markedly reduced particle size, optimal dispersibility, maximized specific surface area, and smooth surfaces were obtained. Photocatalytic degradation experiments confirmed that these optimized samples exhibited significantly enhanced degradation rate constants for model pollutants MO and TC. This study systematically elucidates the multifaceted mechanisms of OA in the synergistic control of TiO₂'s crystalline phase, morphology, and size. It provides a technical pathway for developing highly efficient and stable TiO₂ photocatalysts, thereby advancing their practical applications in environmental remediation.

2. Methods

2.1. Materials

Methyl orange (MO, CAS: 547-58-0, 96%), tetracycline (TC, CAS: 60-54-8, 98%), tetrabutyl titanate (TBOT, CAS: 5593-70-4, 98%), absolute ethanol (CAS: 64-17-5, 99.5%), and oxalic acid (OA, CAS: 144-62-7, 99%) were sourced from Shanghai Aladdin Biochemical Technology Co., Ltd. Supplementary reagents including ammonium oxalate (AO, CAS: 1113-38-8, 98%), 1,4-benzoquinone (BQ, CAS:106-51-4, 97%), and tert-butanol (TBA, CAS: 75-65-0, 99%) were procured from Shanghai Yien Chemical Technology Co., Ltd. All aqueous solutions utilized deionized water throughout experimental procedures.

2.2. Synthesis of TiO₂ catalysts with controlled morphology

The morphology-controlled synthesis of TiO_2 involves two consecutive steps (**Fig. 1**). In the first step, the synthesis was initiated by introducing 20 mL of anhydrous ethanol and 6.8 mL of TBOT into a three-necked flask while maintaining constant agitation. A designated mass of solid OA and 100 mL of deionized water were subsequently introduced. To control hydrolysis rates and achieve precursor uniformity, the reaction mixture was maintained at 3-5°C in an ice-water bath with intense agitation for 3 hours, subsequently subjected to thermal aging (90°C, 8 h). The precursor mixture was subsequently subjected to ambient temperature aging for about 14 hours, resulting in the formation of a phase-separated liquid system. The milky lower phase obtained after decantation was subjected to oven drying (80°C, 5 h), yielding white precursor solids. In the second step, the precursor material was finely pulverized and thermally treated in air at 650°C (5°C/min ramp rate) with a 2-hour isothermal hold, producing the final TiO_2 photocatalyst powder. Catalysts synthesized at $C_2O_4^{2-}$: Ti^{4+} molar ratios of x:10 is designated as Sx (e.g., S20 denotes $C_2O_4^{2-}$: Ti^{4+} = 20:10). Reagent quantities for individual samples are specified in Table 1.

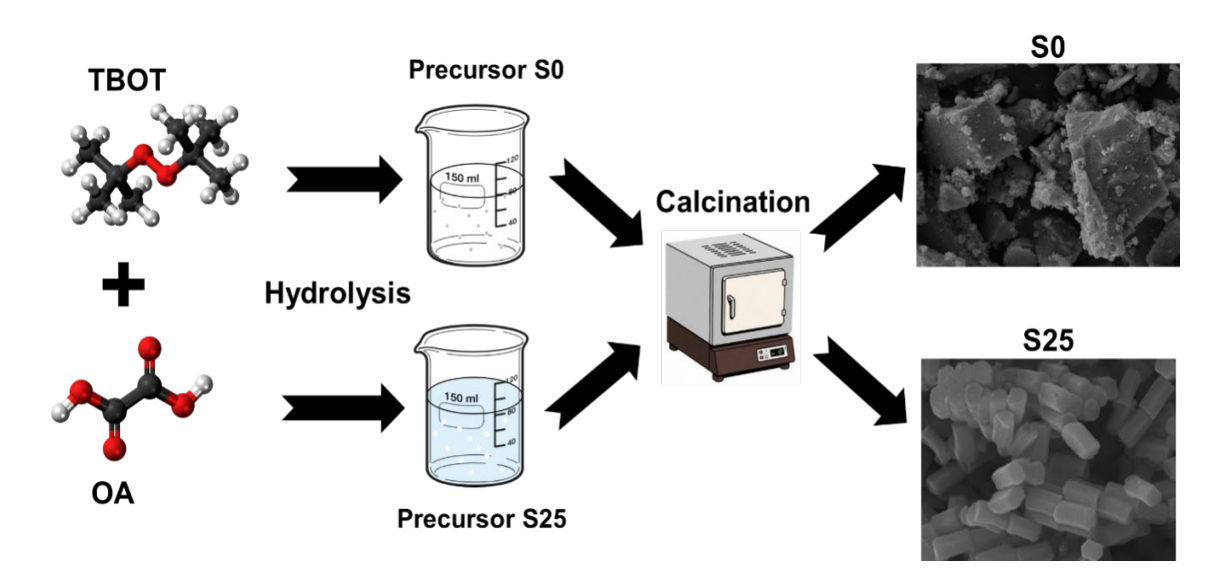


Fig. 1. Preparation process of nanoscale TiO2 with controllable morphology.

Samples	TBOT (mL)	Anhydrous	OA (g)	Water (mL)
1		ethanol (mL)	(2)	
S0	6.8	20	0	100
S5	6.8	20	0.9	100
S10	6.8	20	1.8	100
S20	6.8	20	3.6	100
S25	6.8	20	4.5	100
S30	6.8	20	5.4	100

*Table 1. Dosages of reagents for TiO*₂ morphology control.

2.3. Photocatalytic degradation performance of MO and TC

To simulate natural sunlight, photocatalytic testing was conducted under 300 W Xe-lamp irradiation (100 mW/cm²). In this study, the TiO₂ sample (50 mg) was introduced into 20 mL of MO solution (20 mg/L), while 25 mg was used for TC solution (20 mg/L). Adsorption-desorption balance at TiO₂-pollutant interfaces was established through 30 min magnetic stirring under light-free conditions before photocatalytic initiation. Then, photocatalytic reactions were initiated by illuminating the suspensions. For kinetic profiling of MO degradation, reaction aliquots (1.5 mL) were periodically withdrawn every ten minutes. For TC degradation analysis, sampling was performed every 5 min. Sampled aliquots underwent centrifugation (10,000 rpm, 10 min) to isolate supernatant from photocatalyst particulates. The supernatant (containing residual pollutants) was analyzed using a UV-vis spectrophotometer at $\lambda = 470$ nm for both MO and TC. The degradation ratio (D, %) was calculated according to equation (1):

$$D = \frac{A_0 - A_t}{A_0} \times 100\% = \frac{C_0 - C_t}{C_0} \times 100\%$$
 (1)

Initial supernatant absorbance (A_0) and concentration (C_0) are defined in Equation (1). Conversely, absorbance (A_t) and concentration (C_t) of the solution are measured at irradiation time t. The degradation experiment in this paper conforms to the first-order kinetic model, as shown in equation (2):

$$\ln\left(\frac{C_0}{C_t}\right) = \ln\left(\frac{A_0}{A_t}\right) = kt \tag{2}$$

In the equation, k represents the reaction constant (min⁻¹).

2.4. Scavenger test

The active species were explored in TiO_2 photocatalysts that play a key role in the photocatalytic degradation process. Adding different scavengers eliminates specific radicals in the reaction, allowing a comparison of photocatalytic efficiency changes to determine each radical's role. In the reaction system, AO, BQ, and TBA can trap holes (h⁺), superoxide radicals (\cdot O₂⁻), and hydroxyl radicals (\cdot OH), respectively.

2.5. Characterization

Microstructural characterization employed a FEI scanning electron microscope (SEM; Hillsboro, USA). Crystalline phase analysis utilized a Dandong Haoyuan X-ray diffractometer (XRD; China). Charge carrier behavior was assessed through photoluminescence spectroscopy (PL) using a Hitachi F-4600 fluorometer (Japan). Specific surface areas were determined via Brunauer-Emmett-Teller (BET) measurements (Mike Instruments, Atlanta, GA, USA) based on N₂ adsorption-desorption isotherms.

3. Results and discussion

3.1. The impact of OA on TiO2 morphology

This research employed SEM to investigate oxalic acid's influence on TiO_2 morphological features. When there was no OA or only a trace amount in the reaction system, the S0 and S5 samples (Fig. 2a-d) showed an irregular morphology, with particle sizes ranging from 0.5 to 10 μ m. The particles were irregular polyhedrons and blocks, with rough surfaces and scattered smaller particles. SEM images of S10 sample were shown in Fig. 2(e, f). According to statistical data, the particle size of S10 was 2.47±0.15 μ m. These particles were uniform in size and well-dispersed, with a prismatic shape, slightly rough surfaces, and some cracks.

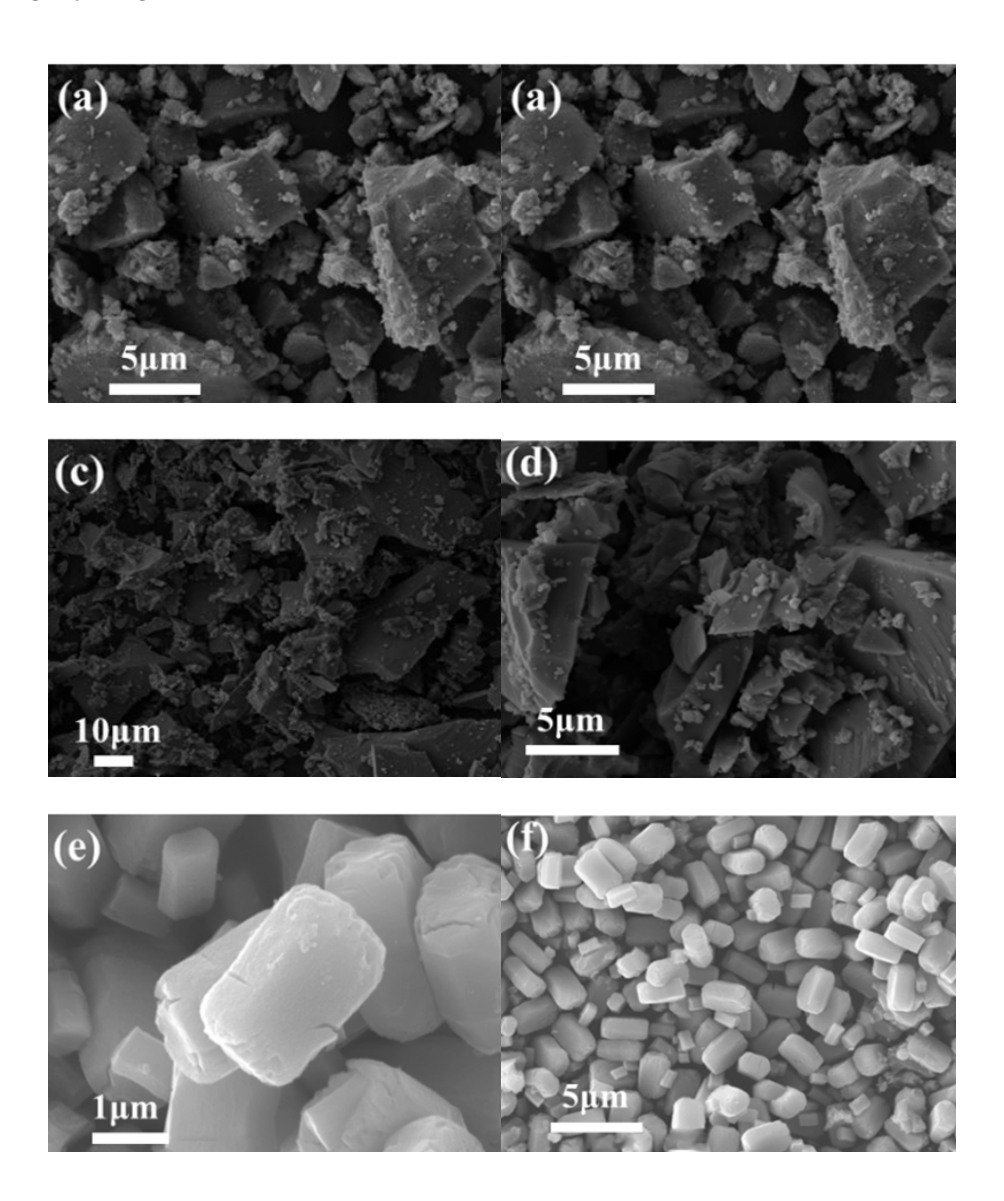


Fig. 2. SEM images of morphology - controlled TiO_2 : (a, b) S0, (c, d) S5 and (e, f) S10.

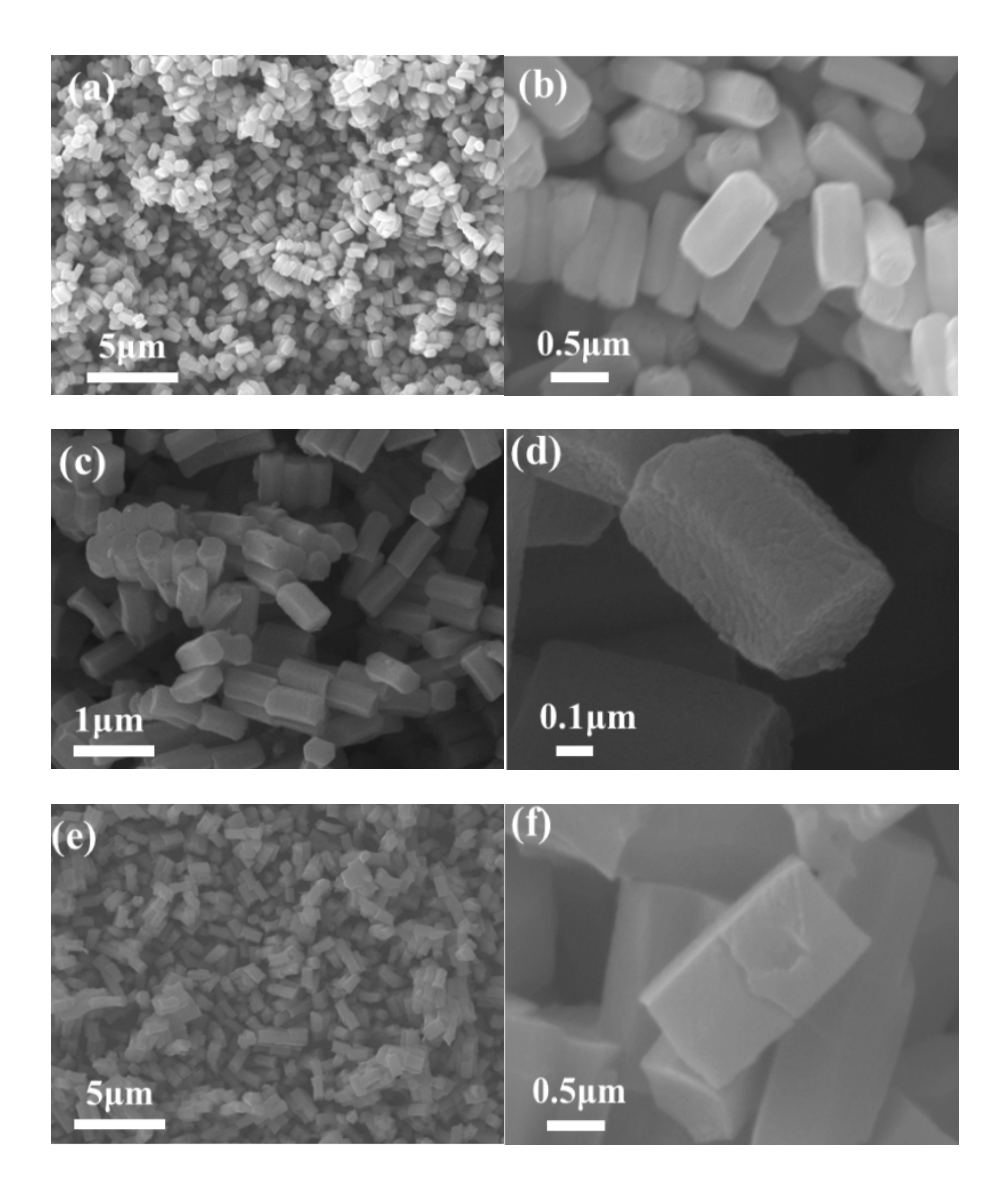


Fig. 3. SEM images of morphology - controlled TiO₂: (a, b) S20, (c, d) S25, and (e, f) S30.

The SEM images of S20 samples were shown in Fig. 3(a, b), where the particles tend to agglomerate and distribute in small blocks. The size of S20 particles was measured $0.82 \pm 0.02~\mu m$ and resemble smooth hexagonal prisms. In Fig. 3(c, d), the S25 samples show reduced agglomeration, with a more uniform surface and particle size of $0.60 \pm 0.03~\mu m$. In Fig. 3(e, f), the S30 samples have a relatively even distribution and particle size of $1.01 \pm 0.05~\mu m$. These particles are slightly rough hexagonal prisms with minor cracks. Thus, the particle size decreased to nanoscale and the morphology became more regular hexagonal prismatic with increasing $C_2O_4^{2-}$: Ti^{4+} to 25:10. With further addition of OA, the particle size increased and etched surfaces of the hexagonal prisms were obtained.

3.2. The influence of OA on crystalline structure of TiO₂

XRD analysis was used to examine the TiO₂ crystal structures. XRD patterns for TiO₂ catalysts prepared under different S conditions (650°C) appear in Fig. 4. The results confirms that

the titanium oxalate precursor exclusively yields rutile-phase TiO₂ following 650°C calcination in the absence of oxalic acid modification. However, when OA was added to the reaction system, even after the same calcination process, the TiO₂ remained in the anatase phase, demonstrating that OA significantly increased the phase transformation temperature of TiO₂. Additionally, as the amount of OA in the reaction system increased, the intensity of the samples' characteristic diffraction peaks also increased, indicating enhanced crystallinity of TiO₂. When the S value reached 25, the diffraction peak intensity and crystallinity peaked. Further increasing the S value led to a decline in crystallinity.

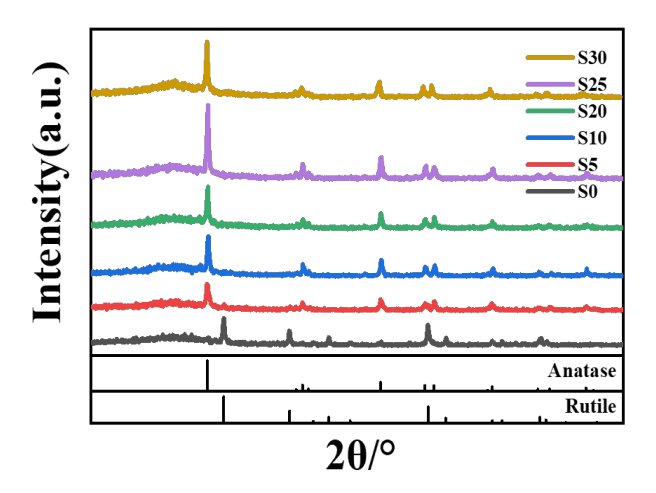


Fig. 4. X-ray diffraction (XRD) patterns of the samples.

3.3. The photocatalytic performance of TiO₂ regulated by OA

Photocatalytic activity of OA-modified TiO₂ was further evaluated through degradation experiments employing TC as the colored dye. Following 30-min dark-phase adsorption equilibrium, TC absorbance spectra were monitored at 5-min intervals during illumination (Fig. S1). Significant dark-reaction activity – encompassing adsorption and degradation processes occurred consistently in all TiO₂ systems. Under light irradiation, TC's absorbance decreased significantly. The photocatalytic TC degradation profile is graphically presented in Fig. 5(a). After 15 minutes in the dark, the D values of the samples were 9.4%, 12.1%, 32.7%, 28.6%, and 24.9%. After 10 min irradiation, degradation efficiencies reached 87.5%, 85.8%, 84.6%, 100%, and 100% respectively. This further confirms that enhanced photocatalytic performance of calcined TiO₂ directly correlates with elevated oxalic acid content in the precursor synthesis. First-order kinetics plots for S0, S10, S20, S25, and S30 are presented in Fig. 5(b). Based on the first-order kinetic model from equation (2), the rate constants were determined to be 0.2193 min⁻¹ for S10, 0.1265 min⁻¹ for S20, 0.3082 min⁻¹ for S25, and 0.2960 min⁻¹ for S30. S25 demonstrated the highest rate constant, exceeding S10 by a factor of 1.40, S20 by 2.43×, and S30 by 1.04×.

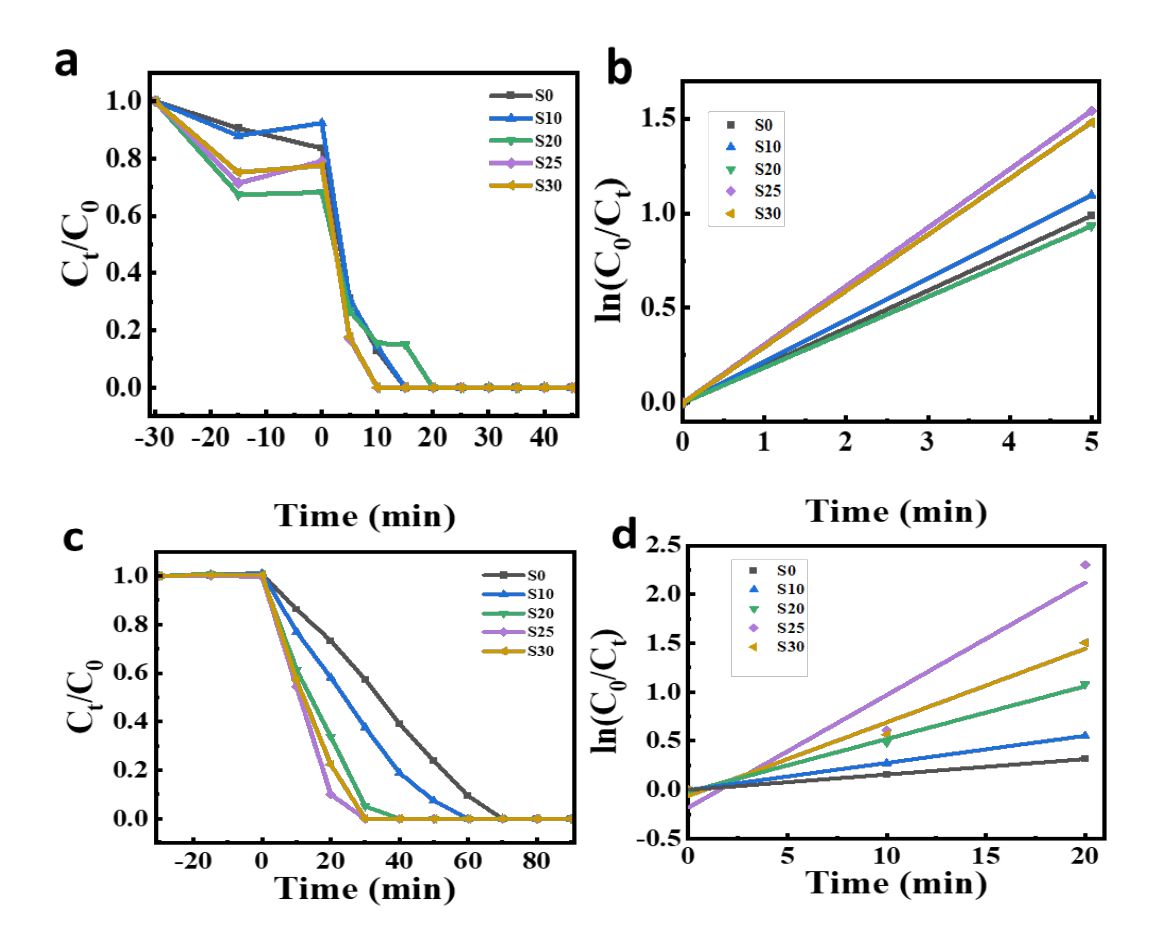


Fig. 5. (a) Degradation curves of TC over S0, S10, S20, S25, and S30 photocatalysts, (b) Corresponding first-order kinetics curves. (c) MO degradation curves; (d) First-order kinetics curves.

To evaluate the photocatalytic performance of TiO₂ with OA addition, degradation experiments using MO as the colored dye were conducted. The temporal changes in absorbance during MO degradation over morphology-controlled S10, S20, S25, and S30 photocatalysts are displayed in Fig. S2. The results indicate that the TiO₂ photocatalysts prepared via the modified method exhibit significant catalytic effects under simulated sunlight. However, S10, S20, and S30 show lower degradation efficiency than S25. From the degradation rate curve in Fig. 5(c), under simulated sunlight for 20 minutes, the degradation efficiencies of S10, S20, S25, and S30 were 41.2%, 66.2%, 90.0%, and 77.7%, respectively. After 30 minutes, these efficiencies reached 62.4%, 94.8%, 100%, and 100%. These results demonstrate that OA regulation not only controls the morphology of the samples but also enhances their performance. Fig. 5(d) presents the first-order kinetics plots of S0, S10, S20, S25, and S30. The linear fitting of these curves, indicative of firstorder kinetics, shows a direct proportionality between the degradation rate and the concentration of the simulated pollutant. Based on the first-order kinetic model from equation (2), the rate constants were determined to be 0.0277 min⁻¹ for S10, 0.0539 min⁻¹ for S20, 0.1151 min⁻¹ for S25, and 0.0752 min⁻¹ for S30. S25 exhibits the highest rate constant, exceeding S10 by a factor of 4.15, S20 by 2.13×, and S30 by 1.53×. These findings confirm that OA can effectively regulate the particle size of TiO₂ and significantly enhance the catalytic degradation efficiency.

3.4. Analysis of photocatalytic reaction mechanism

Generally, reduced particle dimensions enhance specific surface area, thereby exposing additional catalytically active sites. The particle size distribution of all samples is presented in Fig. 6(a). SEM image analysis reveals that under specific conditions, as the amount of OA increases, the TiO₂ particles become more uniform and their size reduces from the micro- to nanometer scale. At S25, the particles are the most uniform and smallest. However, when S reaches 30, the particle surface roughens and size increases. BET measurements reveal that oxalic acid modification tailors both specific surface area and porous architecture of TiO₂. As shown in Fig. 6(b), without OA, TiO₂ demonstrates a specific surface area of 4.04 m²/g.

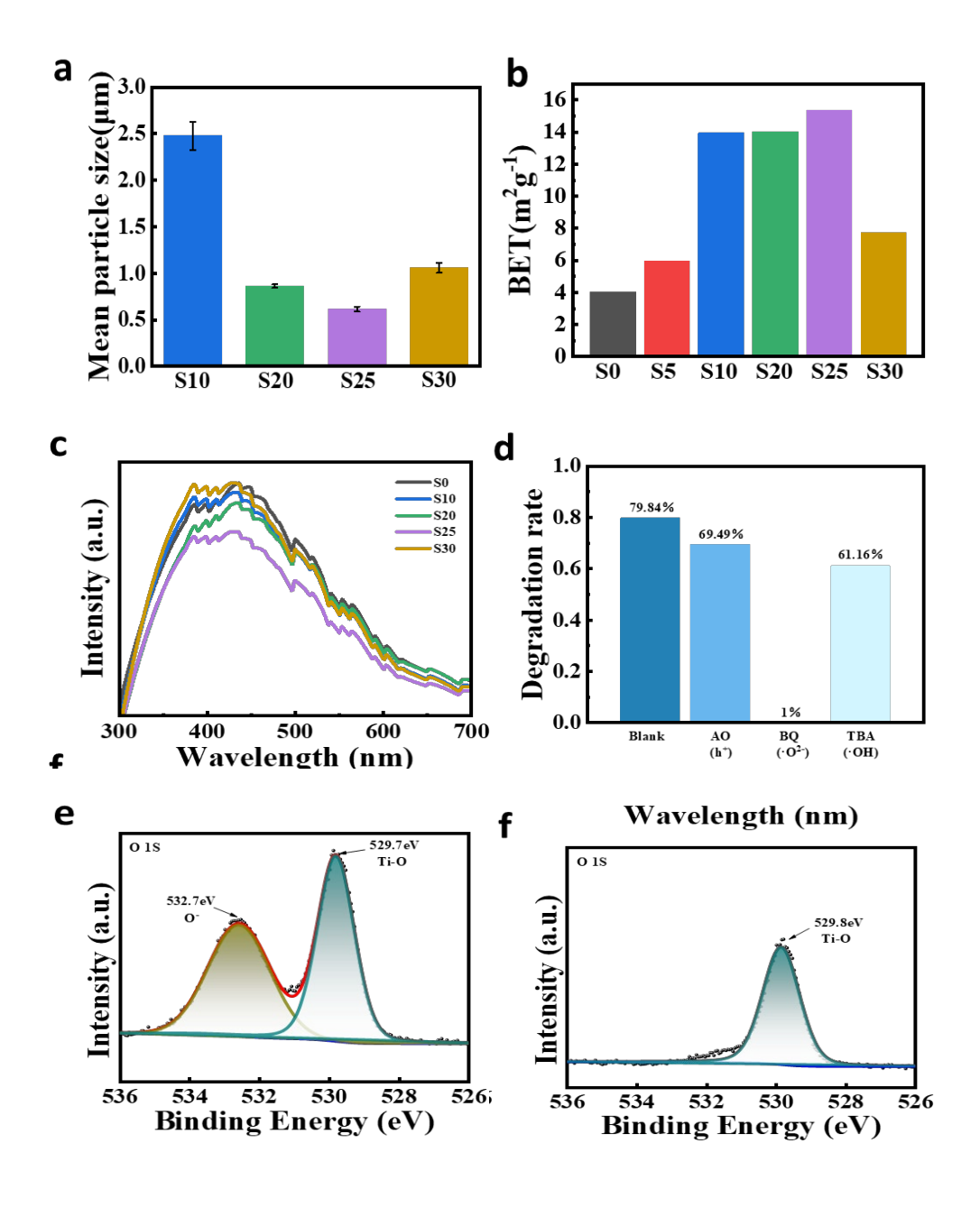


Fig. 6. Characterization of regular TiO₂. (a) Particle size distribution, (b) Specific surface area, (c) PL spectra of the samples, (d) Radical scavenging experiments of S25, and (e, f) O1s spectra of S0 and S25.

With OA addition, the area increases to 5.97, 13.93, 14.02, 15.35, and 7.71 m²/g for different samples. S25 has the highest specific surface area, suggesting more reaction sites and potentially better photocatalytic performance. Under identical experimental conditions, more reaction sites enable a higher reaction capacity within the same timeframe, thereby enhancing photocatalytic activity. These findings are consistent with S25 exhibiting the highest surface area and smallest particle size among all samples. PL was employed to investigate oxalic acid's influence on charge carrier recombination dynamics in TiO₂. As shown in Fig. 6(c), among the TiO₂ samples with different morphologies, the PL intensity peak of the sample prepared with an S value of 25 is the lowest. These results demonstrate minimized charge carrier recombination in S25, corresponding to optimal photogenerated charge separation efficiency among all samples. The experimental results once again confirm that OA introduction can influence the charge carrier recombination efficiency in TiO₂ photocatalysts.

The degradation results of S25 with different radical scavengers are presented in Fig. 6(d). Without any scavenger, the degradation efficiency of MO reached 79.84% after 15 minutes of photocatalytic reaction. After adding AO, the degradation efficiency decreased to 69.49%. The introduction of BQ and TBA as radical scavengers severely suppressed degradation efficiencies to 1% and 61.16%, respectively. This indicates that among the active species, ·O₂- (trapped by BQ) serve as the predominant reactive species, while h⁺ and ·OH also contributed to the photocatalytic degradation, though to a lesser extent.

XPS (Fig. S3) characterization of S0 and S25 samples, indicating that the samples contain carbon, oxygen, and titanium. The detected carbon signal originates either from ambient surface contamination or the carbon-based sample holder employed during XPS measurements. All spectra were charge referenced to C 1s (284.8 eV). As illustrated in Fig. 6(e, f), the O1s binding energies for S0 were 529.7 eV and 532.27 eV. For S25, it was 529.8 eV. The 532.7 eV peak represents adsorbed oxygen (O⁻)[28], whereas lattice oxygen (Ti-O) appears at 529.7 eV and 529.8 eV[29]. For the S25 sample, the disappearance of adsorbed oxygen species may be attributed to the chelation between C₂O₄²⁻ and Ti⁴⁺, which induces a negatively charged TiO₂ surface that repels cationic oxygen-containing pollutants in the environment[30]. In the Ti 2p spectra (Fig. S4(a,c)), the Ti 2p_{3/2} (458.5 eV) and Ti 2p_{1/2} (464.2 eV) binding energies confirm the presence of Ti⁴⁺ in TiO₂ [31]. In the C 1s spectra (Fig. S4(b,d)), the binding energies of 284.8 eV and 288.8 eV for S0 and S25 correspond to C–C and C=O bonds[32, 33]. This suggests the carbon signal mainly originates from contamination during testing.

4. Conclusions

This study demonstrates OA as an effective green modulator for multi-dimensional control of TiO₂ photocatalysts. OA simultaneously stabilizes the anatase phase against high-temperature transformation (retaining pure anatase at 650 °C) and directs the evolution of morphology from irregular polyhedrons to uniform hexagonal prisms. At the optimal $C_2O_4^{2-}$: T_1^{4+} molar ratio of 25:10 (S25), T_1O_2 achieves nanoscale particle size ($0.60 \pm 0.03 \, \mu m$), minimized agglomeration, maximized specific surface area ($15.35 \, \text{m}^2/\text{g}$), and reduced electron-hole recombination. These structural advantages translate to superior photocatalytic performance: S25 degrades 100% of MO within 30 min and 100% of TC within 10 min, exhibiting rate constants ($0.1151 \, \text{min}^{-1}$ for MO, $0.3082 \, \text{min}^{-1}$

for TC) $4.15\times$ and $1.40\times$ higher than OA-free samples, respectively. Mechanistic studies confirm $\cdot O_2^-$ as the primary active species, while XPS analysis reveals OA-induced surface charge modulation that repels cationic pollutants. This work resolves the challenge of synergistic morphology-phase-size control in TiO_2 synthesis using an eco-friendly approach, advancing its practical application in pollutant degradation.

Acknowledgments

This research was funded by Natural Science Foundation of Sichuan Province(2024NSFSC1119) and Qingdao New Energy Shandong Laboratory Open Project (QNESL OP 202303).

References

- [1] F. F. A. Aziz, A. A. Jalil, N. S. Hassan, A. A. Fauzi, M. S. Azami, N. W. C. Jusoh, R. Jusoh, Environmental Research, **209** (2022) 112748; https://doi.org/10.1016/j.envres.2022.112748.
- [2] Y. Li, S. Guo, L. Zhao, S. Chen, Y. Li, X. Yang, P. Wang, W. Feng, Z. Mou, H. Jiang, H. Wei, G. Cerullo, Carbon, **233** (2025) 119923; https://doi.org/10.1016/j.carbon.2024.119923.
- [3] X. Yang, D. Wang, ACS Applied Energy Materials, **1** (12) (2018) 6657-6693; https://doi.org/10.1021/acsaem.8b01345.
- [4] Y. Li, Y. Li, L. Zhao, S. Chen, S. Guo, X. Yang, P. Wang, K. Li, F. Lei, W. Feng, Z. Mou, H. Wei, Journal of Environmental Chemical Engineering, **12** (3) (2024) 112762; https://doi.org/10.1016/j.jece.2024.112762.
- [5] R. Katal, S. Masudy-Panah, M. Tanhaei, M. H. D. A. Farahani, H. Jiangyong, Chemical Engineering Journal, **384** (2020) 123384; https://doi.org/10.1016/j.cej.2019.123384.
- [6] X. Chen, A. Selloni, Chemical Reviews, **114** (19) (2014) 9281-9282; https://doi.org/10.1021/cr500422r.
- [7] J. Schneider, M. Matsuoka, M. Takeuchi, J. Zhang, Y. Horiuchi, M. Anpo, D. W. Bahnemann, Chemical Reviews, **114** (19) (2014) 9919-9986; https://doi.org/10.1021/cr5001892.
- [8] N. S. Allen, N. Mahdjoub, V. Vishnyakov, P. J. Kelly, R. J. Kriek, Polymer Degradation and Stability, **150** (2018) 31-36; https://doi.org/10.1016/j.polymdegradstab.2018.02.008.
- [9] L. Yang, M. Gong, X. Jiang, D. Yin, X. Qin, B. Zhao, W. Ruan, Journal of Raman Spectroscopy, **46** (3) (2015) 287-292; https://doi.org/10.1002/jrs.4645.
- [10] A. Testino, I. R. Bellobono, V. Buscaglia, C. Canevali, M. D'Arienzo, S. Polizzi, R. Scotti, F. Morazzoni, Journal of the American Chemical Society, **129** (12) (2007) 3564-3575; https://doi.org/10.1021/ja067050+.
- [11] C. Liu, Y. Qin, W. Guo, Y. Shi, Z. Wang, Y. Yu, L. Wu, Applied Surface Science, **580** (2022) 152262; https://doi.org/10.1016/j.apsusc.2021.152262.
- [12] P. Reñones, A. Moya, F. Fresno, L. Collado, J. J. Vilatela, V. A. de la Peña O'Shea, Journal of CO2 Utilization, **15** (2016) 24-31; https://doi.org/10.1016/j.jcou.2016.04.002.
- [13] S. Chen, D. Li, Y. Liu, W. Huang, Journal of Catalysis, **341** (2016) 126-135; https://doi.org/10.1016/j.jcat.2016.06.016.

- [14] M. Maiti, M. Sarkar, S. Maiti, M. A. Malik, S. Xu, Journal of Cleaner Production **255** (2020) 120183; https://doi.org/10.1016/j.jclepro.2020.120183.
- [15] D. Li, H. Song, X. Meng, T. Shen, J. Sun, W. Han, X. Wang, Nanomaterials, **10** (3) (2020) 546; https://doi.org/10.3390/nano10030546.
- [16] Z. Zhang, C.-C. Wang, R. Zakaria, J. Y. Ying, The Journal of Physical Chemistry B, **102** (52) (1998) 10871-10878; https://doi.org/10.1021/jp982948+.
- [17] M. Pal, J. García Serrano, P. Santiago, U. Pal, The Journal of Physical Chemistry C, **111** (1) (2007) 96-102; https://doi.org/10.1021/jp0618173.
- [18] H. Yang, B. Yang, W. Chen, J. Yang, Catalysts, **12** (10) (2022) 1263; https://doi.org/10.3390/catal12101263.
- [19] X. Zheng, Q. Kuang, K. Yan, Y. Qiu, J. Qiu, S. Yang, ACS Applied Materials & Interfaces, **5** (21) (2013) 11249-11257; https://doi.org/10.1021/am403482g.
- [20] M. Andrade-Guel, L. Díaz-Jiménez, D. Cortés-Hernández, C. Cabello-Alvarado, C. Ávila-Orta, P. Bartolo-Pérez, P. Gamero-Melo, Boletín de la Sociedad Española de Cerámica y Vidrio, **58** (4) (2019) 171-177; https://doi.org/10.1016/j.bsecv.2018.10.005.
- [21] L.-L. Sui, Y.-C. Zhai, L.-H. Miao, Rare Metals, **34** (12) (2015) 895-900; https://doi.org/10.1007/s12598-014-0359-3.
- [22] H. Zhang, Y. Wang, P. Liu, Y. Han, X. Yao, J. Zou, H. Cheng, H. Zhao, ACS Applied Materials & Interfaces, **3** (7) (2011) 2472-2478; https://doi.org/10.1021/am200363p.
- [23] Y.-J. Gu, M. Zhou, Z. Dong, Z. Cheng, T.-S. Deng, Journal of Physics: Conference Series, **1885** (3) (2021) 032012, https://doi.org/10.1088/1742-6596/1885/3/032012.
- [24] J.-P. Nikkanen, T. Kanerva, T. Mäntylä, Journal of Crystal Growth, **304** (1) (2007) 179-183; https://doi.org/10.1016/j.jcrysgro.2007.02.012.
- [25] G. H. Guai, Q. L. Song, Z. S. Lu, C. M. Ng, C. M. Li, Renewable Energy, **51** (2013) 29-35; https://doi.org/10.1016/j.renene.2012.08.078.
- [26] K. Khosravi, M. E. Hoque, B. Dimock, H. Hintelmann, C. D. Metcalfe, Analytica Chimica Acta, **713** (2012) 86-91; https://doi.org/10.1016/j.aca.2011.11.048.
- [27] X. Chen, S. S. Mao, Chemical Reviews, **107** (7) (2007) 2891-2959; https://doi.org/10.1021/cr0500535.
- [28] F. Güzelçimen, B. Tanören, Ç. Çetinkaya, M. D. Kaya, H. İ. Efkere, Y. Özen, D. Bingöl, M. Sirkeci, B. Kınacı, M. B. Ünlü, S. Özçelik, Vacuum, **182** (2020) 109766; https://doi.org/10.1016/j.vacuum.2020.109766.
- [29] N. Kar Chowdhury, B. Bhowmik, Materials Today: Proceedings, **56** (2022) 984-988; https://doi.org/10.1016/j.matpr.2022.03.113.
- [30] X. Kong, Y. Xu, Z. Cui, Z. Li, Y. Liang, Z. Gao, S. Zhu, X. Yang, Applied Catalysis B: Environmental, **230** (2018) 11-17; https://doi.org/10.1016/j.apcatb.2018.02.019.
- [31] V. A. Bardin, Y. A. Vorotnikov, I. P. Asanov, N. A. Vorotnikova, M. A. Shestopalov, Applied Surface Science, **612** (2023) 155738; https://doi.org/10.1016/j.apsusc.2022.155738.
- [32] S. A. Abdullah, M. Z. Sahdan, N. Nayan, Z. Embong, C. R. C. Hak, F. Adriyanto, Materials Letters, **263** (2020) 127143; https://doi.org/10.1016/j.matlet.2019.127143.
- [33] M. Pisarek, M. Krawczyk, M. Hołdyński, W. Lisowski, ACS Omega, **5** (15) (2020) 8647-8658; https://doi.org/10.1021/acsomega.0c00094.